

Supporting Information

Ag/Ni-MOF Heterostructure with Synergistic Enrichment and Activation Properties for Electrocatalytic Reduction of 4-nitrophenol

Huaiquan Zhao, Xuliang Pang, Yifei Huang, Yajie Bai, Jinrui Ding, Hongye Bai*, Weiqiang Fan*

^a School of Chemistry and Chemical Engineering, Jiangsu University, Zhenjiang, 212013, PR China.

*Corresponding authors: bhy198412@163.com, fwq4993329@ujs.edu.cn.

Experimental section

1. Chemicals and reagents

Nickel nitrate hexahydrate ($\text{Ni}(\text{NO}_3)_2 \cdot 6\text{H}_2\text{O}$), 1,3,5-trimesic acid (BTC), tributylmethylammonium methyl sulfate (MTBS), N, N-dimethylformamide (DMF), silver nitrate (AgNO_3), 4-nitrophenol (4-NP), 4-aminophenol (4-AP), potassium hydroxide (KOH), sodium borohydride (NaBH_4), and carbon tetrachloride (CCl_4) were purchased from Sinopharm Chemical Reagent Co., Ltd in China. Distilled water was used throughout the experiment. The thickness of nickel foam (NF) was 1.5 mm.

2. Synthesis of Ni-MOF/NF

The electrochemical deposition was operated in a three-electrode cell, with the pre-treated NF ($1 \times 2 \text{ cm}^2$), platinum wire, and Ag/AgCl electrode as the working electrode, counter electrode, and reference electrode, respectively. 0.654 g $\text{Ni}(\text{NO}_3)_2 \cdot 6\text{H}_2\text{O}$, 1.05 g BTC and 1.56 g MTBS (supporting electrolyte) were dissolved in 50 mL DMF as the electrolyte. The electrochemical deposition was carried out at -1.5 V vs. Ag/AgCl for 800 s. (Fig. S1)¹. The obtained samples were washed with distilled water and ethanol, respectively. Finally, the samples were dried in an oven at 60 °C for 12 h.

3. Synthesis of Ag/Ni-MOF/NF

Ag nanosheets were decorated on Ni-MOF by the in-situ deposition. The prepared Ni-MOF/NF was immersed in 3 mM AgNO_3 aqueous solution for 5 h to realize the deposition of Ag nanosheets. The synthesized samples were rinsed with distilled water, and subsequently placed in an oven at 60 °C for 12 h.

4. Characterization

The morphology of samples was characterized by a scanning electron microscope (SEM, Hitachi S-4800). The fine structure was investigated by transmission electron microscopy (TEM, Tecnai G2 F20 S-Twin electron microscope). X-ray diffraction (XRD, Bruker D8 ADVANCE X-ray diffractometer) was used to characterize the crystal structure. The functional groups of samples were studied by Fourier transform infrared spectroscopy (FT-IR, Nexus 470, Thermo Electron Corporation). X-ray photoelectron spectroscopy (XPS, Thermo Fisher Scientific) was used to investigate the valence state of elements. Qualitative and quantitative research on production was

performed by the ultraviolet-visible (UV-vis) absorption spectrometer (Agilent Technologies Cary 8454 UV-Vis).

5. Electrochemical experiments

All the electrochemical tests were investigated by CHI 660E electrochemical workstation in a three-electrode system, where Ag/Ni-MOF/NF, Hg/HgO electrode, and platinum tablet acted as the working electrode, reference electrode, and counter electrode, respectively. The linear sweep voltammograms (LSVs) were carried out in a voltage range of 0–1.1 V vs. Hg/HgO with a sweep rate of 5 mV·s⁻¹. The sealed electrolyzers were injected with 40 mL 1.0 M KOH, and 0.139 g 4-NP (25 mM) was added to the cathode cell. Ar gas was introduced earlier to remove dissolved oxygen and continued until the end of the 4-NP reduction. The frequency range of electrochemical impedance spectroscopy (EIS) measurements were 0.01–10⁶ HZ.

6. Product analysis

4-NP will deprotonate and transform to 4-NP⁻ anion in an alkaline solution, and this process can be monitored by UV-vis absorption spectra, since the characteristic absorption of 4-NP ($\lambda_{\text{max}}=317$ nm) and 4-NP⁻ ($\lambda_{\text{max}}=400$ nm) are significantly different (Fig. S11).^{2,3} According to the photo of the reaction solution, it can be also observed that the color deepened after the formation of 4-NP⁻ (Fig. S12). Therefore, UV-vis absorbance at $\lambda_{\text{max}}=400$ nm is used as the detecting wavelength for qualitative and quantitative studies on 4-NP conversion. 10 μ L reaction solution was diluted with 3 mL distilled water and 100 μ L 1 M NaBH₄ (to protect the product from oxidation), and the diluted solution was transferred to a quartz cell and further measured by the UV-vis absorption spectrometer. 4-NP performs a UV-vis maximum absorption wavelength at 400 nm ($\lambda_{\text{max}}=400$ nm), and the alternation of absorbance was monitored. The quantitative analysis of related products was determined by the standard curve based on the absorption peak at 400 nm.

The calculation formulas of reaction rate (v), conversion and FE are as follows:

$$v = \frac{(C_0 - C) \times V}{t \times m}$$

$$\text{Conversion (\%)} = \left(1 - \frac{C}{C_0}\right) \times 100 \%$$

$$\text{FE (\%)} = \frac{n_{\text{AP}} \times 6F}{Q} \times 100\%$$

C_0 presents the initial concentration of reactants, C presents the concentration of reactants after reaction, V presents the volume of the reaction solution, t presents the reaction time, m presents the mass of catalyst, n_{AP} presents the amount of 4-AP substance, F presents the Faradaic constant, Q presents the consumed charges.

7. EPR experiments of H radicals

The formation of H radicals was further investigated by the electron paramagnetic resonance (EPR) measurements with 5,5-dimethyl-1-pyrroline N-oxide (DMPO) as the radical spin-trapping reagent. The Ag/Ni-MOF/NF sample were put into the cathodic cell containing 40 mL 1 M KOH with 0.139 g 4-NP. The electrocatalytic reduction of 4-NP was conducted by chronoamperometry at -0.9 V vs. Hg/HgO (optimal potential) for 10 min. Subsequently, the detection solution, which was formed by 50 μL reaction solution and 50 μL DMPO, was tested immediately by EPR.

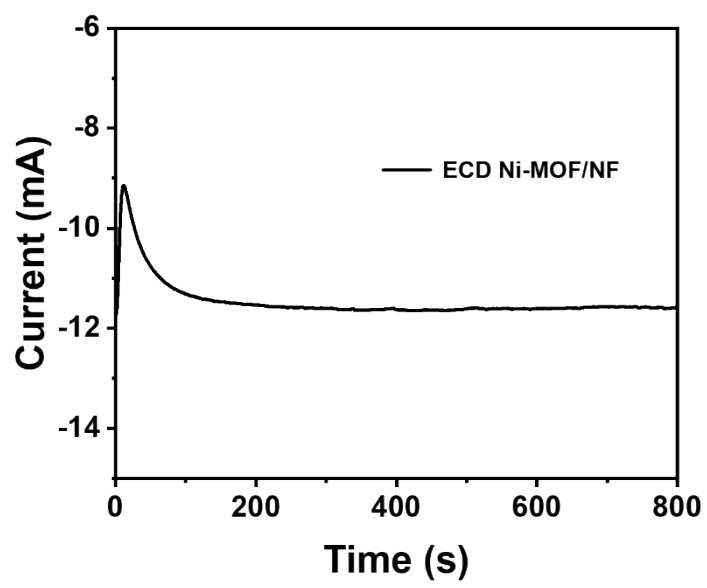


Fig. S1. Electrochemical deposition process of Ni-MOF/NF.

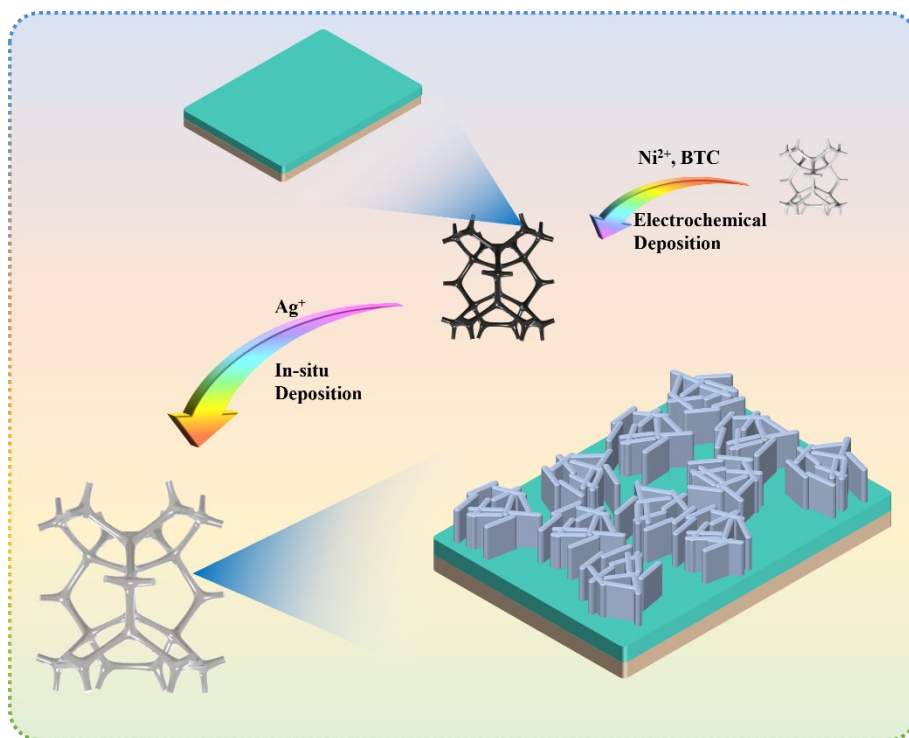


Fig. S2. Synthesis process of Ag/Ni-MOF/NF.

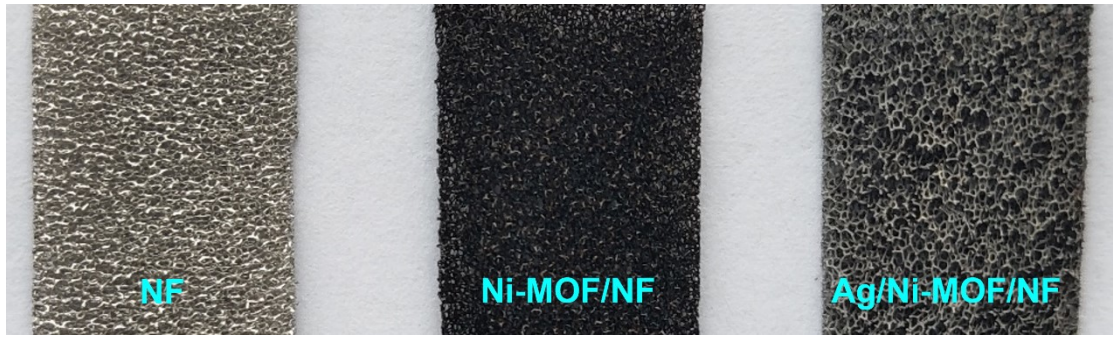


Fig. S3. The pictures of NF, Ni-MOF/NF and Ag/Ni-MOF/NF.

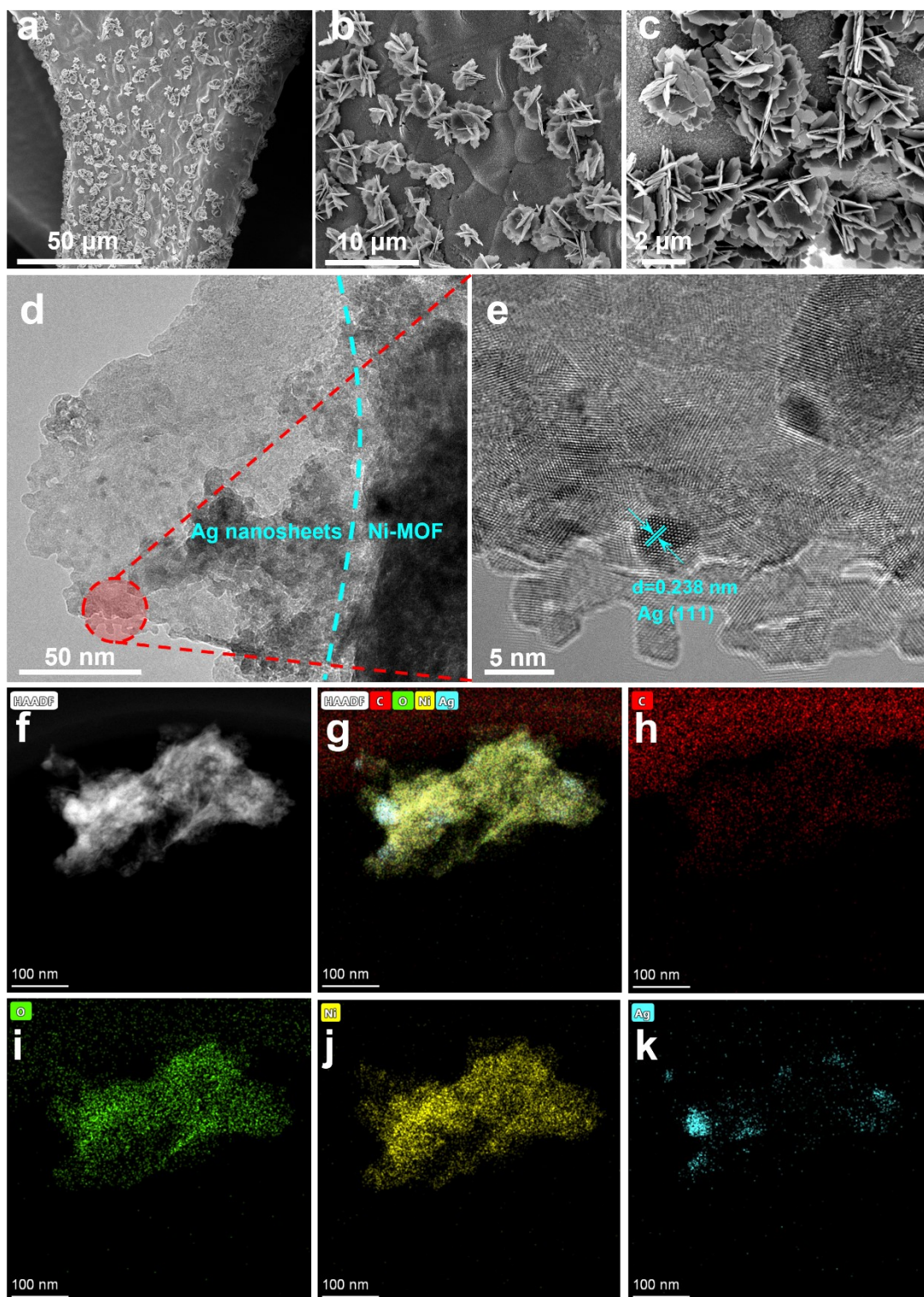


Fig. S4. (a–c) SEM images, (d) TEM image, (e) HRTEM image, (f–k) TEM-EDS elemental mapping images of Ag/Ni-MOF/NF.

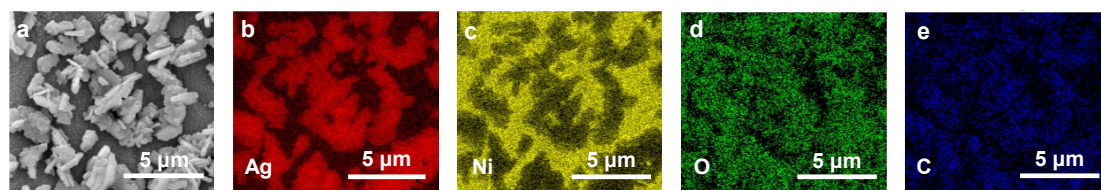


Fig. S5. EDS elemental mapping images of Ag/Ni-MOF/NF.

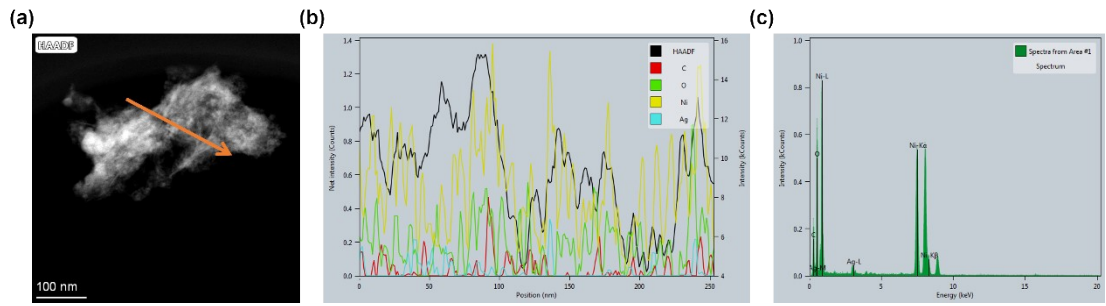


Fig. S6. (a) and (b) EDS line scan curves and (c) EDS face scan curve of Ag/Ni-MOF/NF.

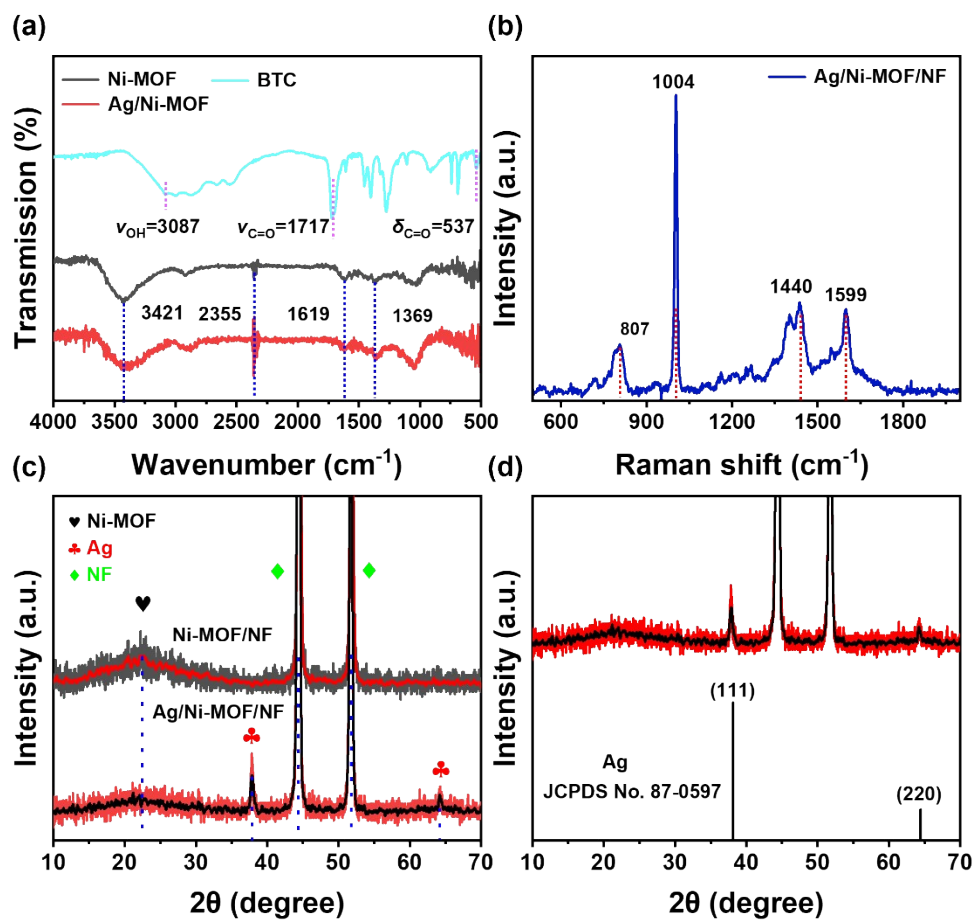


Fig. S7. (a) FT-IR spectroscopies of BTC, Ni-MOF and Ag/Ni-MOF. (b) Raman spectroscopy of Ag/Ni-MOF/NF. (c) XRD patterns of Ni-MOF/NF and Ag/Ni-MOF/NF. (d) XRD pattern of Ag/Ni-MOF/NF.

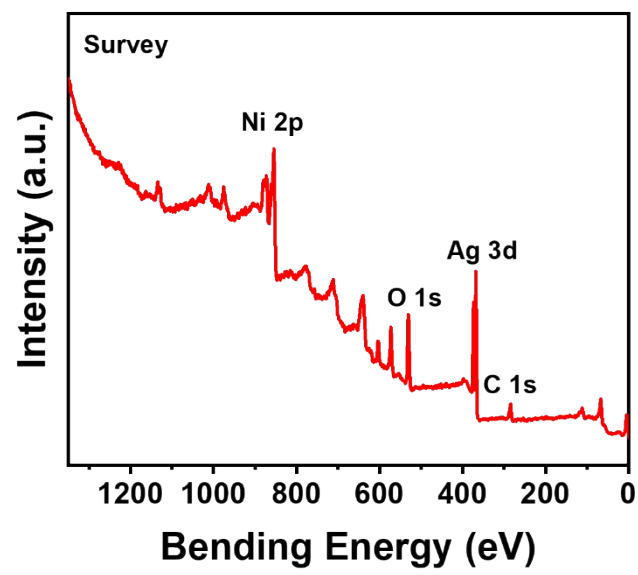


Fig. S8. XPS survey spectrum for Ag/Ni-MOF/NF.

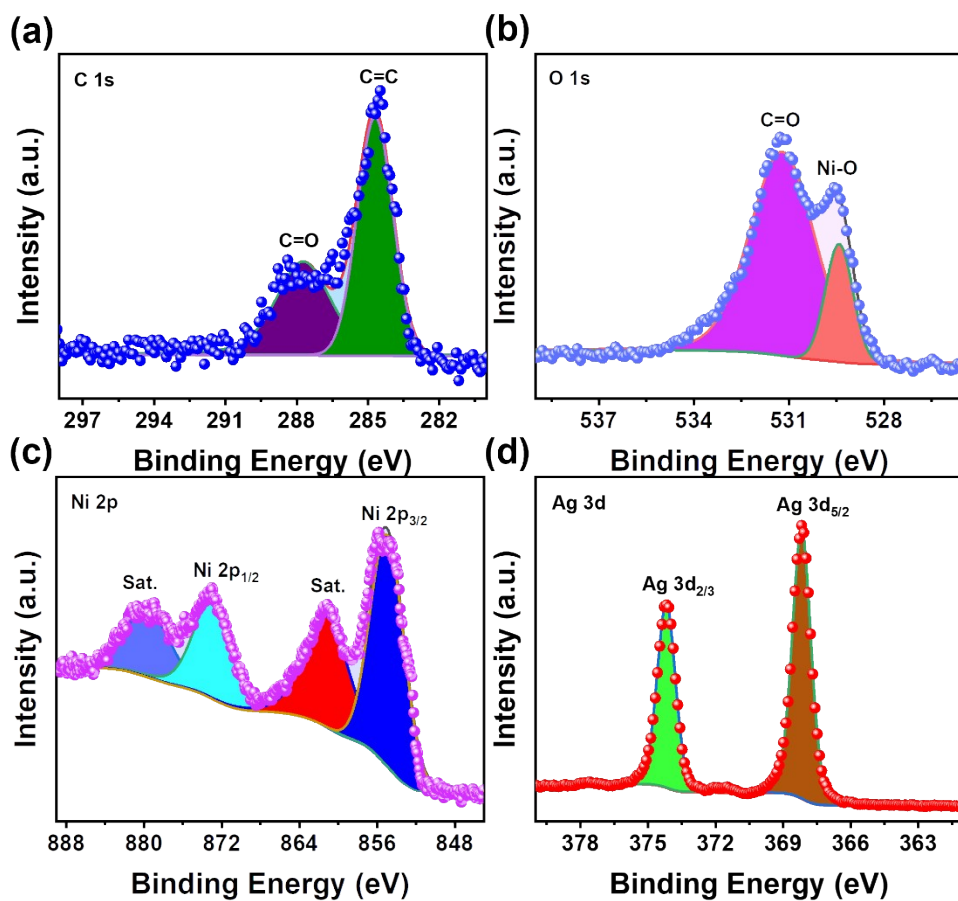


Fig. S9. XPS spectra of Ag/Ni-MOF/NF.

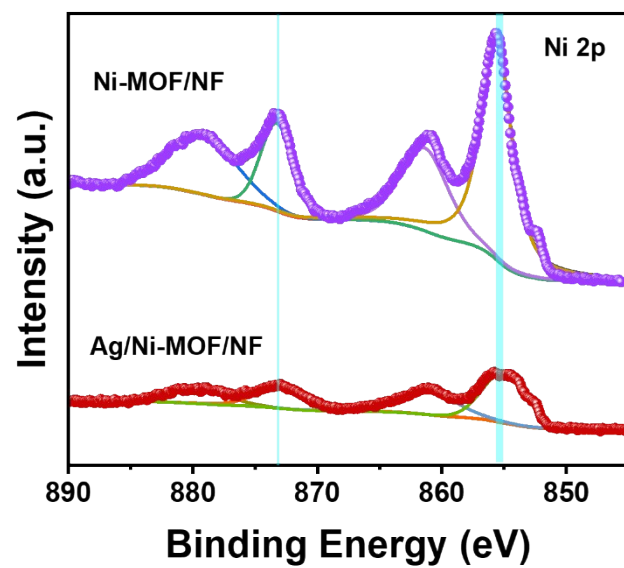


Fig. S10. XPS spectra of Ni 2p orbital for Ni-MOF/NF and Ag/Ni-MOF/NF.

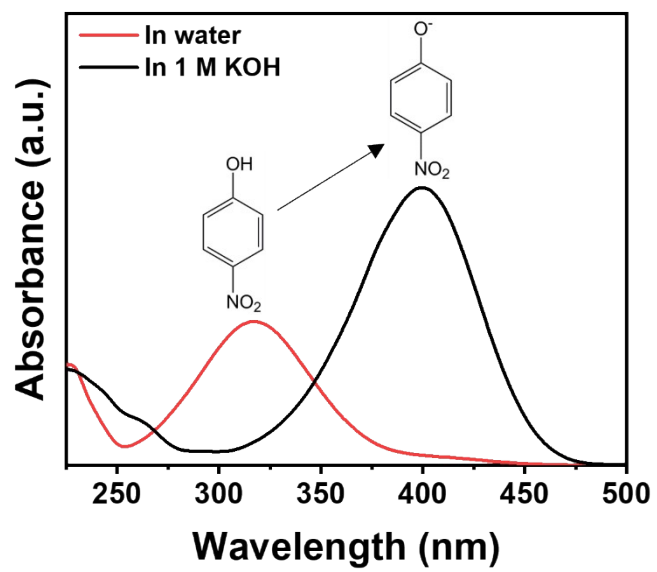
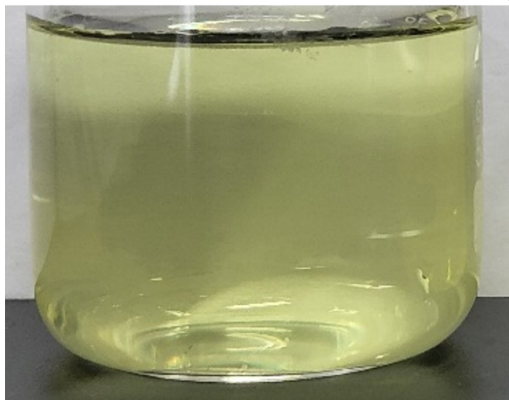


Fig. S11. UV-vis absorption spectra of 4-NP in pure water and 1 M KOH solution, respectively.

(a)



(b)



Fig. S12. 25 mM 4-NP in pure water (a) and 1 M KOH solution (b).

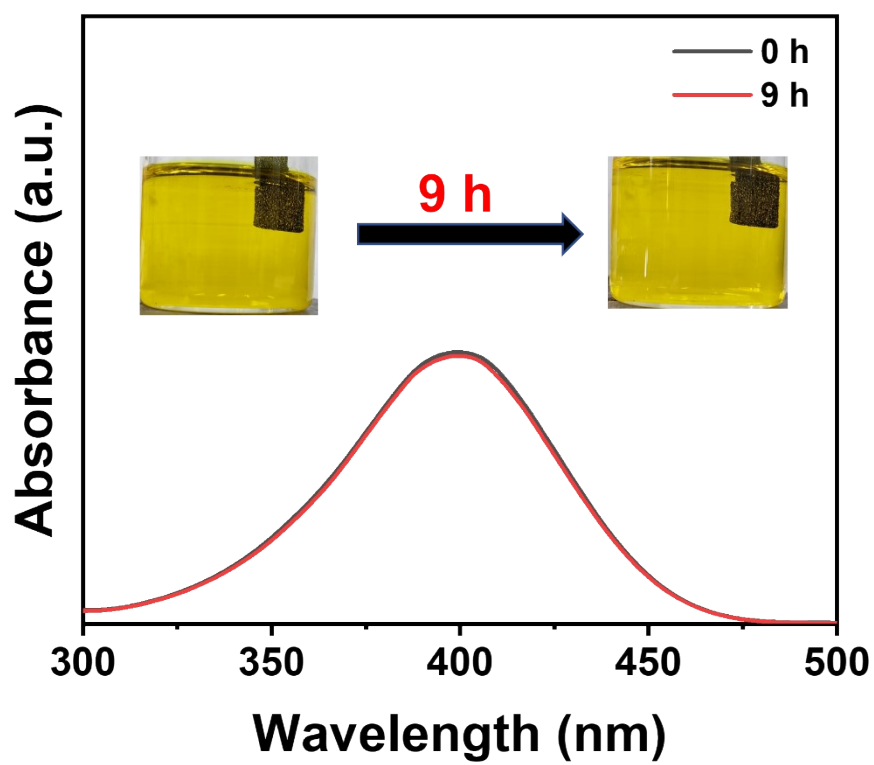


Fig. S13. UV-vis absorption spectra of 25 mM 4-NP and product for 9 h without electric field.

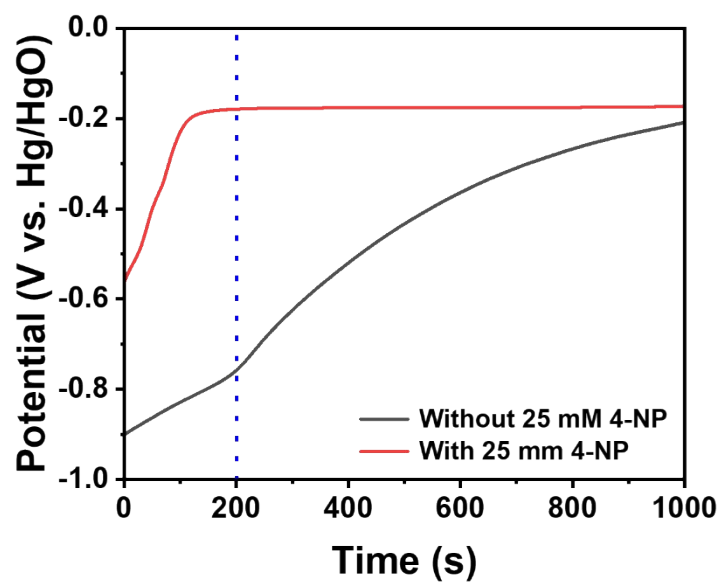


Fig. S14. The open-circuit potential vs. time of the activated Ag/Ni-MOF/NF (Ag/Ni-MOF/NF after being activated by LSV operation) with and without 25 mM 4-NP.

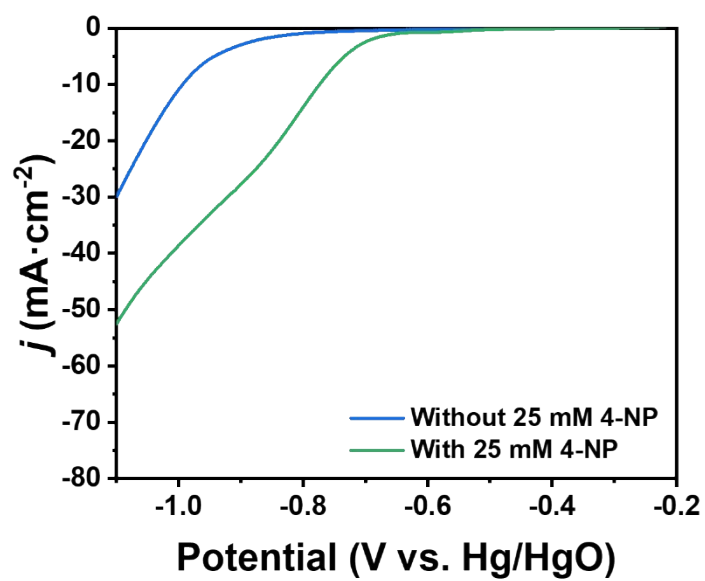


Fig. S15. LSV curves of Ni-MOF/NF with and without 25 mM 4-NP in 1 M KOH.

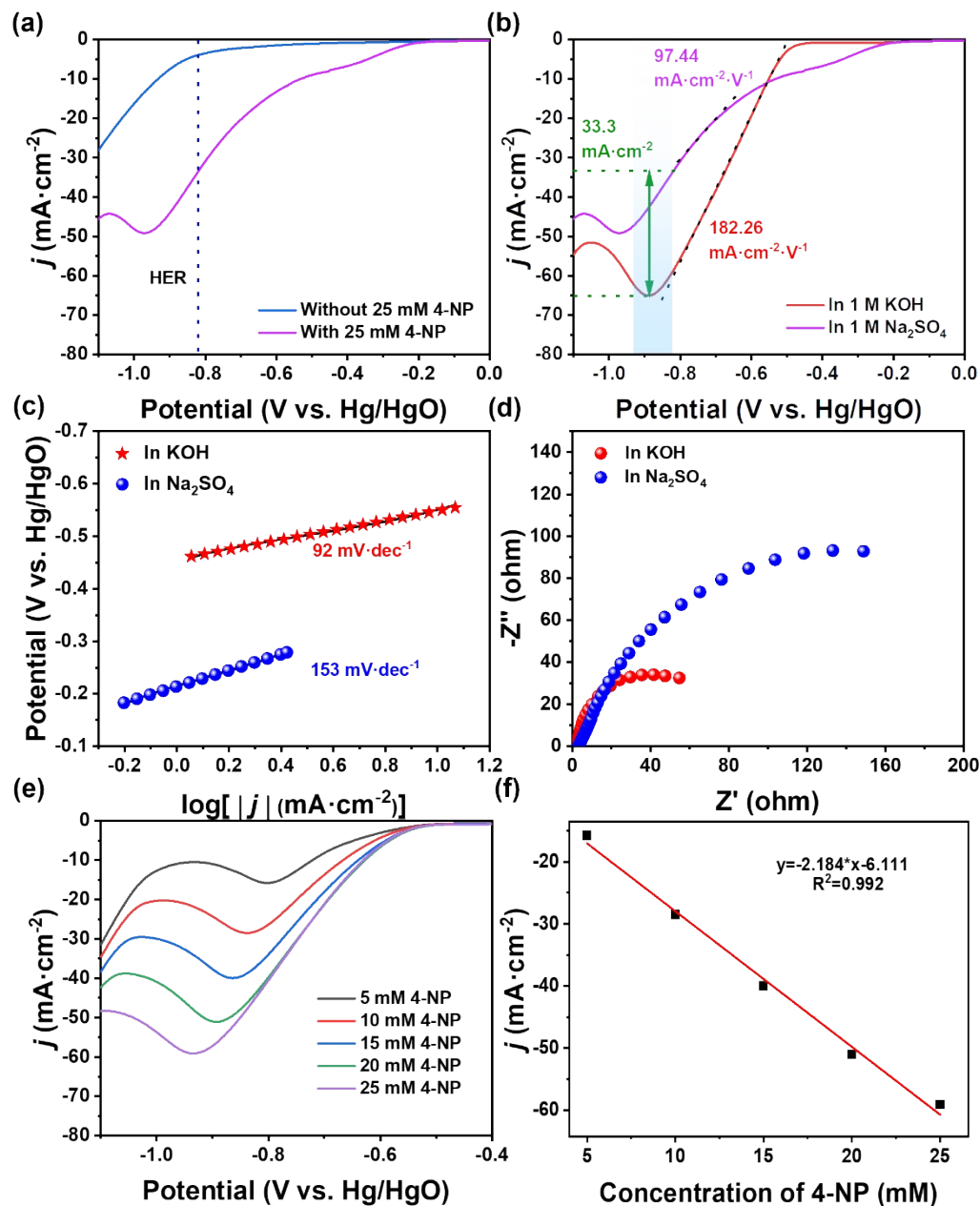


Fig. S16. (a) LSV curves of Ag/Ni-MOF/NF with and without 25 mM 4-NP in 1 M Na₂SO₄. (b) LSV curves, (c) Tafel plots and (d) Nyquist plots of Ag/Ni-MOF/NF in different electrolyte with 25 mM 4-NP. (e) LSV curves of Ag/Ni-MOF/NF in the different concentrations of 4-NP (1 M KOH). (f) Plot of maximum current density vs. concentrations of 4-NP.

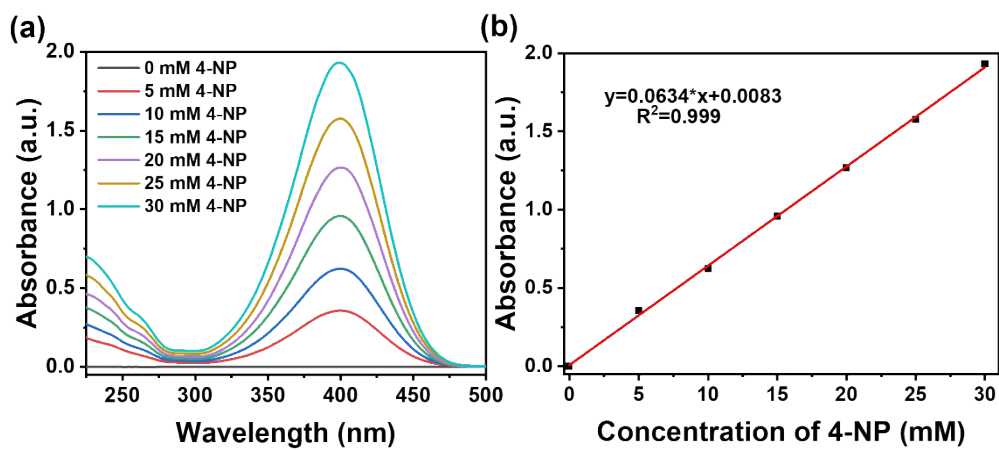


Fig. S17. (a) UV-vis absorption spectra of 4-NP solution with the different concentrations. (b) Standardized curve of UV-vis absorbance ($\lambda_{\text{max}}=400$ nm) vs. concentrations of 4-NP.

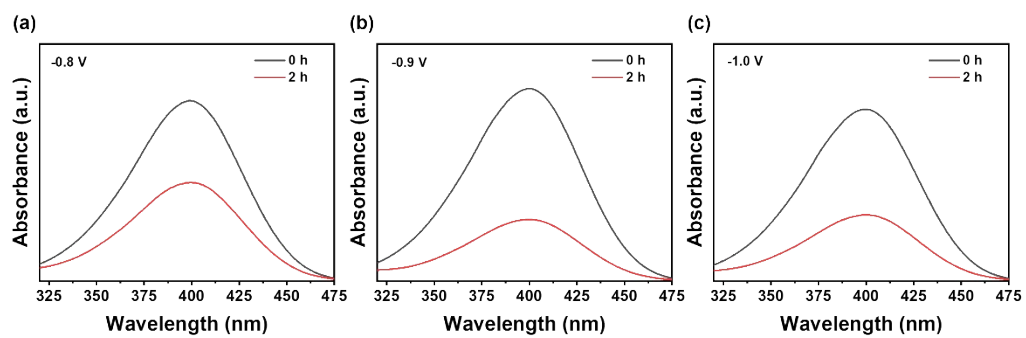


Fig. S18. UV-vis absorption spectra of 25 mM 4-NP and product ($\lambda_{\max}=400$ nm) within 2 h at different potentials.

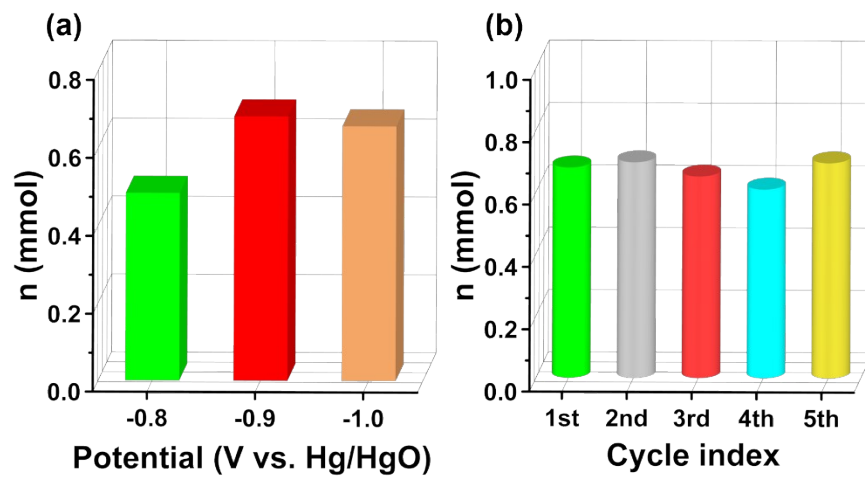


Fig. S19. (a) Consumed amount of 4-NP within 2 h under different potentials. (b) Reusability of Ag/Ni-MOF/NF at -0.9 V vs. Hg/HgO.

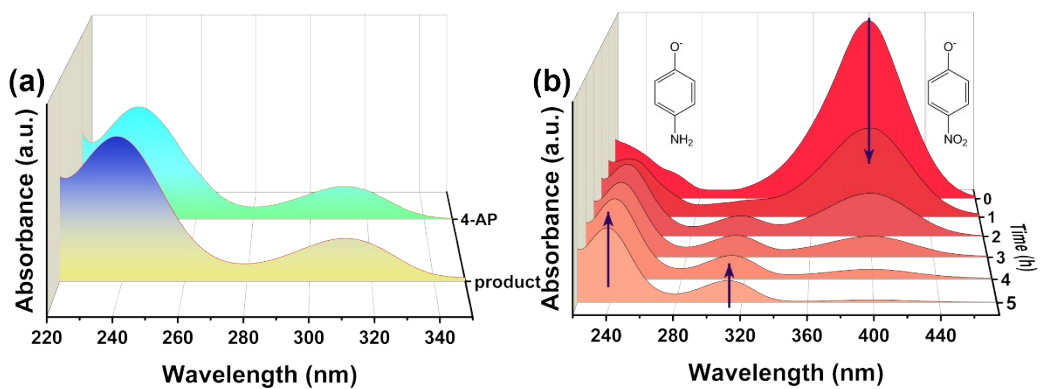


Fig. S20. (a) UV-vis absorption spectra of standard 4-AP and product in 1 M KOH. (b) UV-vis absorption spectra of 4-NP of reaction (1 M KOH, -0.9 V vs. Hg/HgO, initial concentration of 4-NP: 25 mM).

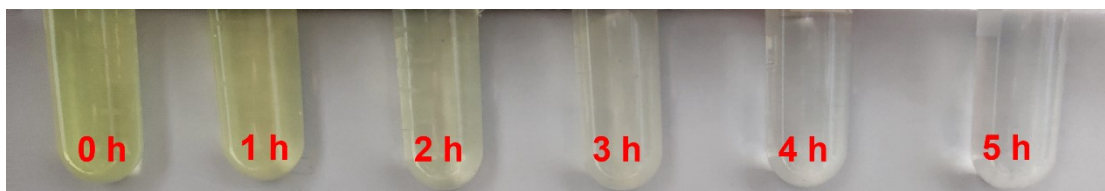


Fig. S21. Color change of solution over time at -0.9 V vs. Hg/HgO (the solution has been diluted from $10\ \mu\text{L}$ to $3\ \text{mL}$).

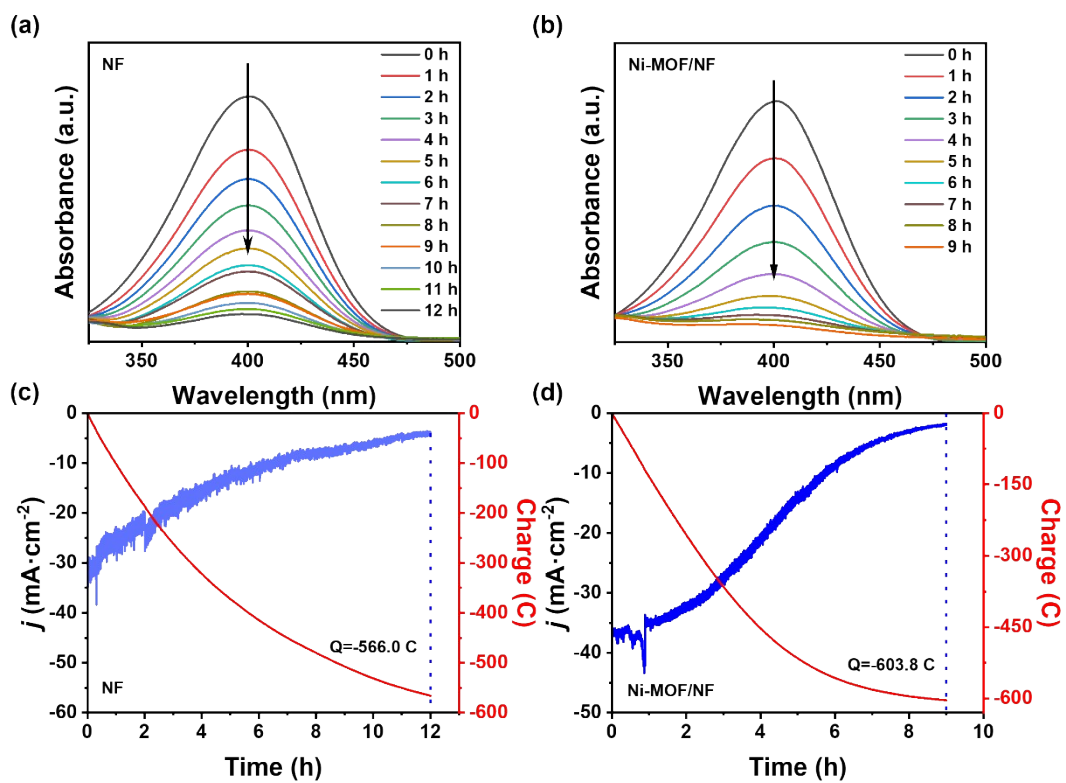


Fig. S22. (a) UV-vis absorption spectra and (c) current density and charge vs. time over NF at -0.9 V vs. Hg/HgO. (b) UV-vis absorption spectra and (d) current density and charge vs. time over Ni-MOF/NF at -0.9 V vs. Hg/HgO.

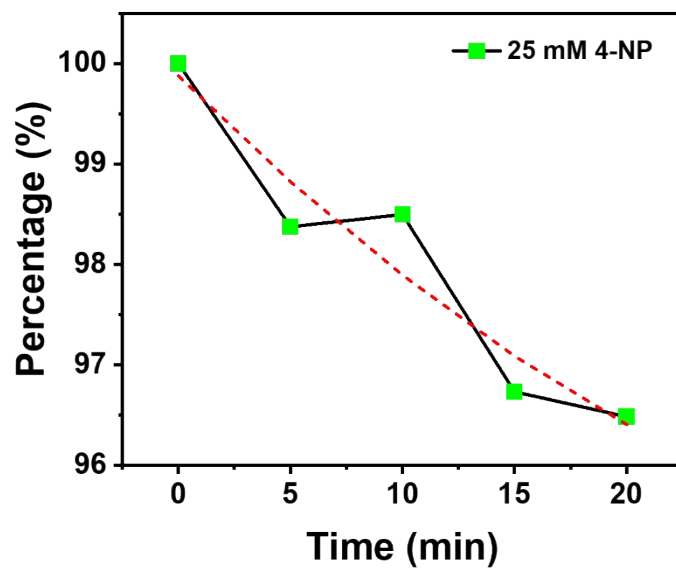


Fig. S23. The change of 4-NP content under Ni-MOF adsorption within 20 min.

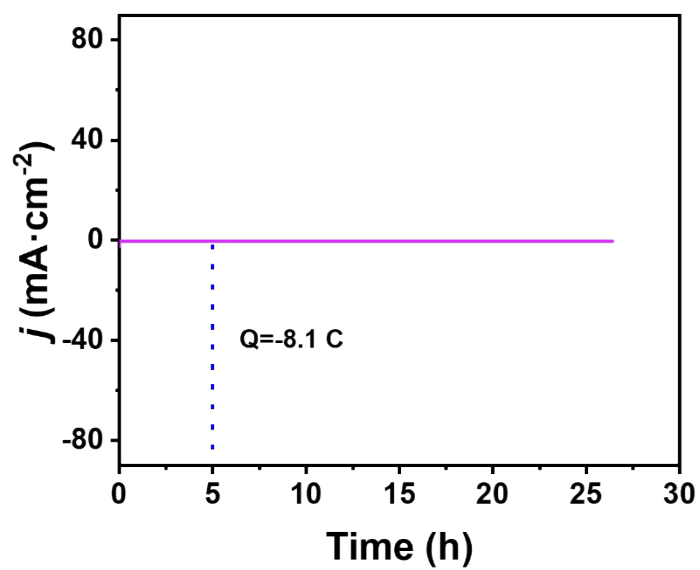


Fig. S24. Current density vs. time under a constant-potential at -0.9 V vs. Hg/HgO without 4-NP.

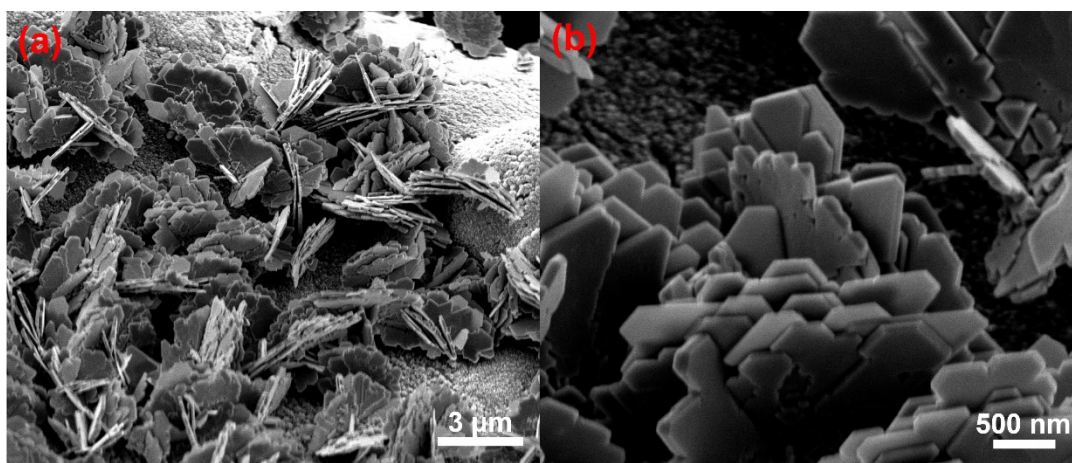


Fig. S25. (a-b) SEM images of Ag/Ni-MOF/NF after electrolysis at -0.9 V vs. Hg/HgO for 5 h.

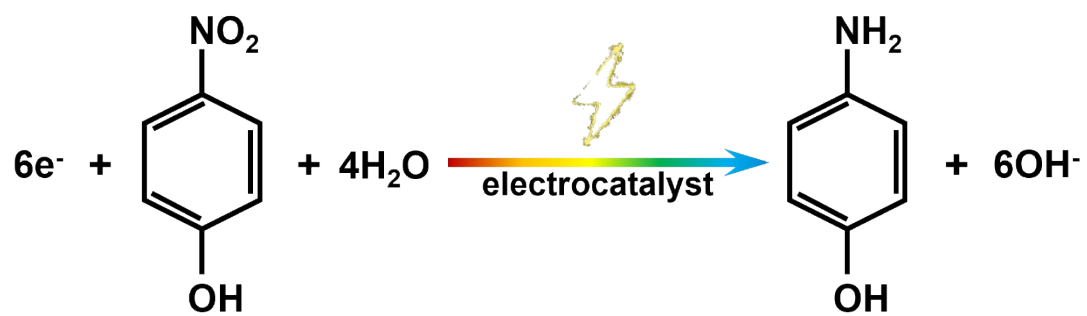


Fig. S26. Equation of electrocatalytic reduction of 4-NP.

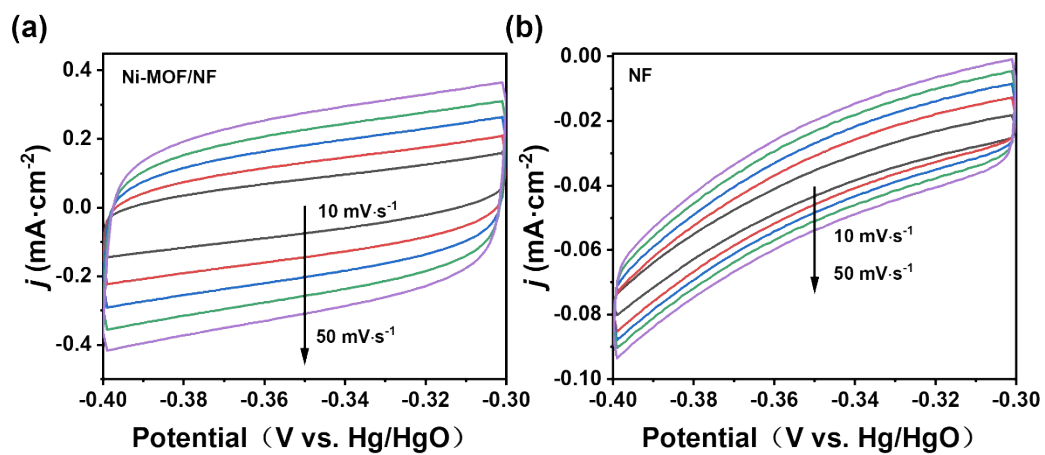


Fig. S27. CV curves of Ni-MOF/NF (a) and NF (b) at different scan rates (25 mM 4-NP).

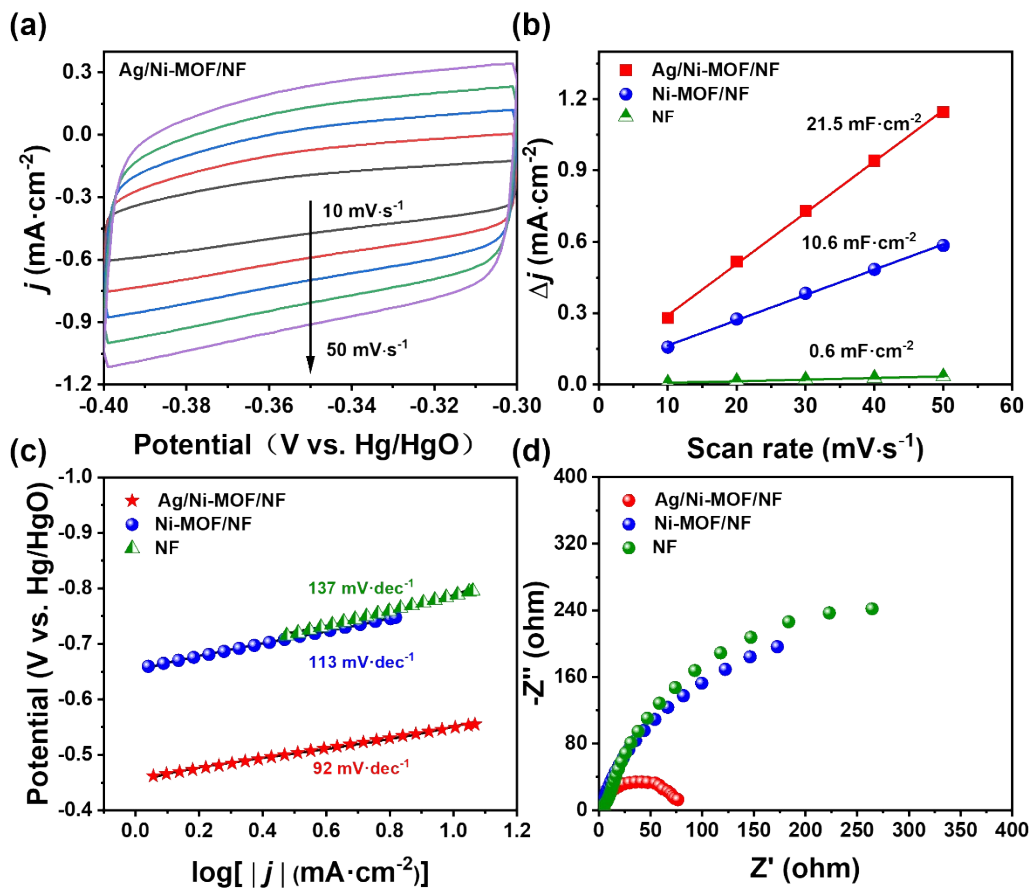


Fig. S28. (a) CV curves of Ag/Ni-MOF/NF at different scan rates. (b) Plots of current density differences vs. scan rates. (c) Tafel plots and (d) Nyquist plots of Ag/Ni-MOF/NF, Ni-MOF/NF, and NF. Measured condition: 25 mM 4-NP (1 M KOH).

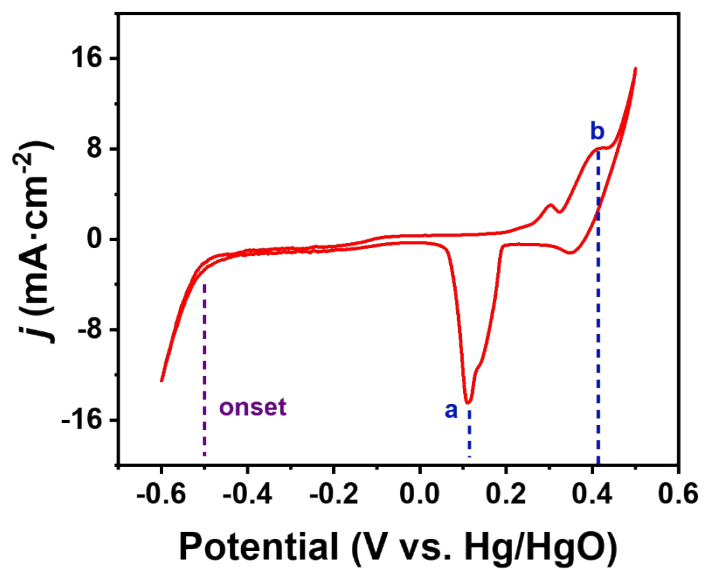


Fig. S29. CV measurements of Ag/Ni-MOF/NF in 1 M KOH (25 mM 4-NP) with a scan rate of $5 \text{ mV}\cdot\text{s}^{-1}$.

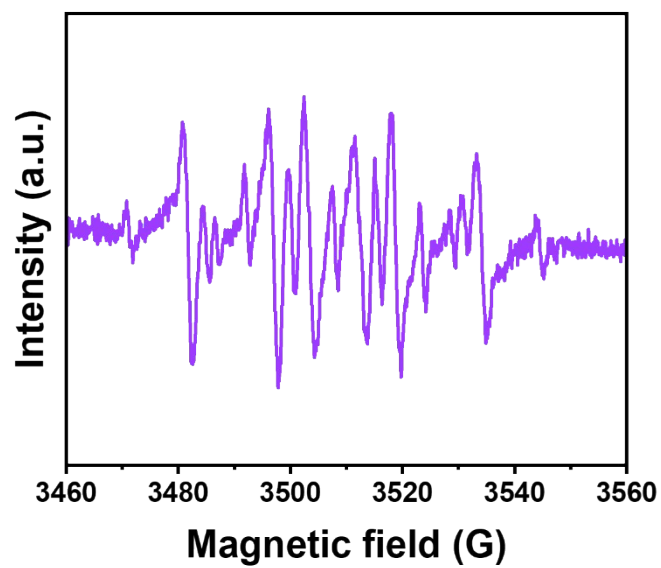


Fig. S30. EPR measurement with 5,5-dimethyl-1-pyrroline N-oxide (DMPO, the radical spin-trapping reagent) for H radicals over the Ag/Ni-MOF/NF.

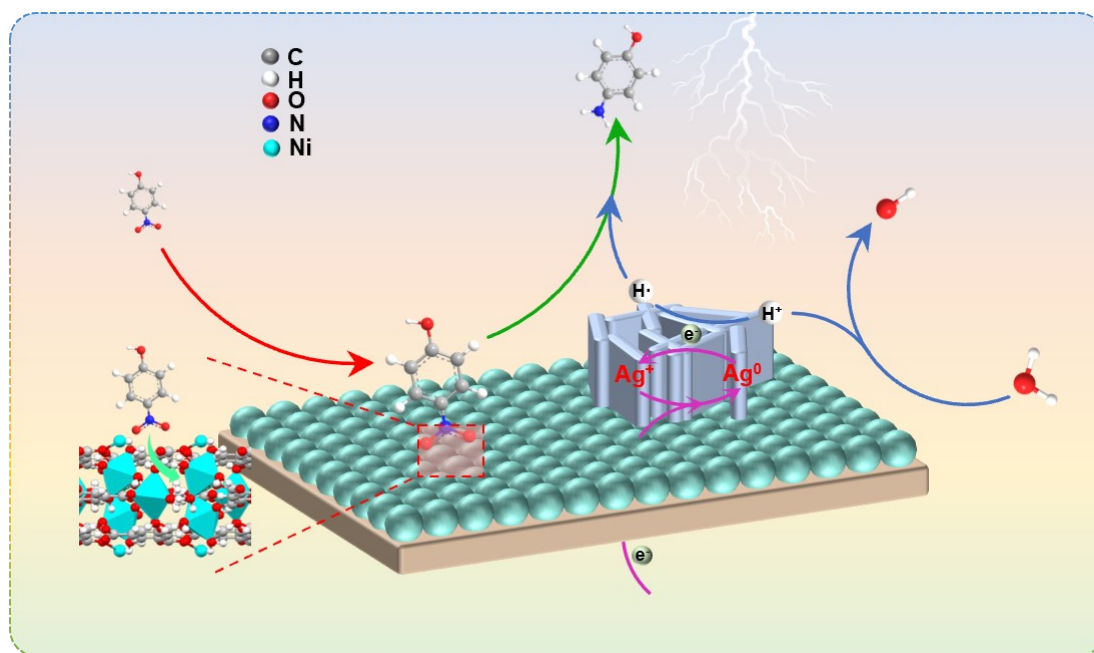


Fig. S31. Schematic diagram of 4-NP electrocatalytic reduction.

Table S1. Some recent work reports on the reduction of 4-NP.

material	catalytic type	sacrificial agent	consumption of 4-NP (μmol)	Reaction rate ($\mu\text{mol}\cdot\text{min}^{-1}\cdot\text{mg}^{-1}$)	reference
$\text{Cu}_{11}\text{H}_3(\text{Tf-dpf})_6(\text{OAc})_2$ (Cu_{11})	Thermal catalysis	NaBH_4	20	2	3
$\text{Fe}_3\text{O}_4@\text{PPy-MAA/Ag}$	Thermal catalysis	NaBH_4	25	0.222	4
$\text{Cu}_{2-x}\text{Si}_2\text{O}_5(\text{OH})_3\cdot x\text{H}_2\text{O}$	Thermal catalysis	NaBH_4	0.5	0.75	5
$\text{Cu}_2\text{O}@\text{ZIF-8}$	Thermal catalysis	NaBH_4	0.313	0.0007	6
ZIF-0/1-700 N	Thermal catalysis	NaBH_4	0.2	0.4	7
$\text{Au}@\text{CuO}_x\text{-CeO}_2$ CSNs	Thermal catalysis	NaBH_4	0.3	3	8
CDs/CuO/mHA	Photocatalysis	NaBH_4	2.16	0.018	9
CaCO_3/CuS	Photocatalysis	NaBH_4	1.96	0.013	10
Ag/Ni-MOF/NF	Electrocatalysis		984	3.168	This work

1. L. Wang, Y. Wu, R. Cao, L. Ren, M. Chen, X. Feng, J. Zhou, B. Wang, *ACS Appl. Mater. Interfaces*, **2016**, 8, 16736-16743.
2. J. Strachan, C. Barnett, A.F. Masters, T. Maschmeyer, *ACS Catal.*, **2020**,10, 5516-5521.
3. C.Y. Liu, S.F. Yuan, S. Wang, Z.J. Guan, D.E. Jiang, Q.M. Wang, *Nat. Commun.*, **2022**, 13, 1-8.
4. R. Das, V.S. Sypu, H.K. Paumo, M. Bhaumik, V. Maharaj, A. Maity, *Appl. Catal. B*, **2019**, 244, 546-558.
5. W. Zhu, P. Sun, W. Ran, Y. Zheng, L. Wang, L. Zhang, X. Jia, J. Chen, J. Wang, H. Zhang, Z. Liu, S. Zhao, *Chem. Eng. J.*, **2021**, 411, 128442.
6. B. Li, J.G. Ma, P. Cheng, *Angewandte Chemie*, **2018**, 130, 6950-6953.
7. X. Liu, L. Wu, T. Liu, L. Zhang, *Appl. Catal. B*, **2021**, 281, 119513.
8. K. Wu, X.-Y. Wang, L.-L. Guo, Y.-J. Xu, L. Zhou, Z.-Y. Lyu, K.-Y. Liu, R. Si, Y.-W. Zhang, L.-D. Sun, C.-H. Yan, *Nano Res.*, **2020**, 13, 2044-2055.
9. Q. Chang, W. Xu, N. Li, C. Xue, Y. Wang, Y. Li, H. Wang, J. Yang, S. Hu, *Appl. Catal. B*, **2020**, 263, 118299.
10. X. Zhang, M. Liu, Z. Kang, B. Wang, B. Wang, F. Jiang, X. Wang, D.-P. Yang, R. Luque, *Chem. Eng. J.*, **2020**, 388, 124304.